An empirical target discharging model relevant to hot-electron preheat in direct-drive implosions on OMEGA

2013 Plasma Phys. Control. Fusion 55 045001

(http://iopscience.iop.org/0741-3335/55/4/045001)

Plasma Phys. Control. Fusion **55** (2013) 045001 (9pp) doi:10.1088/0741-3335/55/4/045001

An empirical target discharging model relevant to hot-electron preheat in direct-drive implosions on OMEGA

N Sinenian, M J-E Manuel, J A Frenje, F H Séguin, C K Li and R D Petrasso

Plasma Science and Fusion Center, Massachusetts Institute of Technology, Cambridge, MA 02139, USA

E-mail: nareg@psfc.mit.edu

Received 14 November 2012, in final form 20 January 2013
Published 21 February 2013
Online at stacks.iop.org/PPCF/55/045001

Abstract
Charging of inertial confinement fusion (ICF) targets generates a potential well that traps energetic electrons within the target. Trapped electrons can preheat the fuel, raise the adiabat, degrade compression and perhaps have an effect on achieving the high areal densities (ρR) required for ignition and gain. The decay time of this potential is thus an important parameter for any calculations of preheat. A nonlinear model of electrical discharging of ICF capsules has been developed and is presented here. The empirical model, which captures the essential dynamics of the target voltage decay, incorporates previous charged-particle spectroscopic and radiographic measurements of the fields surrounding the target. On the basis of this model, it is shown that the decay time is weakly dependent on the initial voltage of the target. In addition, it is shown that currents through the target support fiber aid target discharging. Implications of these findings for inertial fusion energy targets without support fibers are discussed.

(Some figures may appear in colour only in the online journal)

1. Introduction

The charging of inertial confinement fusion (ICF) targets to several hundred kilovolts and the associated acceleration of fast ions due to this potential was first observed in electrically isolated planar targets nearly 35 years ago [1]. In these early experiments, 0.3 cm thick aluminum targets were irradiated with 50 ps laser pulses ($\lambda_L = 1.06\,\mu$m). Electric potentials with peak amplitudes of order 1 kV were measured using a fast-response voltage probe. These potentials had relatively fast rise times (1 ns) and long decay times (10 ns). Charging of the target was attributed to the generation of hot electrons by laser–plasma interactions (LPIs). The fastest of these hot electrons escape, leaving behind a positive potential on the target. The remaining space charge then accelerates ions from the coronal plasma and traps hot electrons that have energies less than the target potential.

After these initial experiments, optical diagnostics were used to qualitatively characterize the currents flowing along the thin fiber or stalk that connects targets to the chamber [2]. In was determined that ionization and subsequent heating of the stalk occur primarily because of the large electric fields across the stalk that ionize the stalk material into a plasma and drive an ohmic current through it.

More recent experiments on OMEGA ($\lambda_L = 0.3\,\mu$m, $\sim$1 ns pulses) [3] found charging of spherical ICF capsules to voltages of order 1 MV [4]. In those experiments, the peak target voltage was inferred from time-integrated spectral measurements of fast ions that were accelerated from the coronal plasma. Energy upshifts of fusion products were also observed and used to infer the time history of the target potential over a fraction of the total voltage decay time [5]. This was achieved by simultaneous measurements of the energy upshift of four different fusion products (DD-p, DD-T, D^3He-p and D^3He-α), which sample the target potential at different times due to their different velocities. It was shown that the target potential had completely decayed several hundred picoseconds after the end of the laser pulse. In addition, it was found that the peak target voltage scales linearly with laser intensity [4] and that the hot electrons responsible for target charging are generated by the two-plasmon-decay (TPD) instability [6, 7].

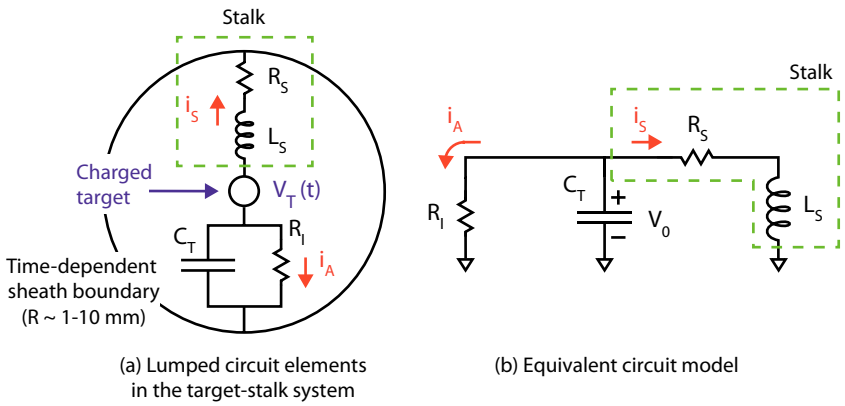

Figure 1. (*a*) The lumped circuit elements representing the target-stalk system at OMEGA. The stalk is composed of an inductor in series with a resistor, while the target is modeled as a capacitor with leakage. The voltage drop is between the target (∼1 mm diameter) and the sheath boundary, which expands radially in time (from ∼1 mm to 1 cm) with the fast ions and hot electrons. (*b*) The corresponding electric circuit. Ground in this circuit corresponds to the potential at the sheath boundary.

Charging of spherical capsules is of concern within the ICF community because it can hinder the achievement of the ρR required for ignition and energy gain. As a fraction of the hot electrons escape the target, they leave behind a positive charge that acts to trap slower (but suprathermal) electrons. These electrons, trapped for a duration that is prescribed by the target potential decay time, can deposit their energy within the target. This electron preheat occurs during the acceleration phase of ICF implosions and raises the fuel adiabat, thereby reducing the optimal ρR [8]. The amount of electron preheat depends on the hot-electron source characteristics (emission angle, energy distribution) as well as the dynamics of the target potential (i.e. how much energy the electrons deposit in the fuel within the decay time).

Experimental investigation of the evolution of the target potential is generally difficult for a number of reasons. First, the aforementioned technique for indirect measurement of the potential time history using charged fusion products is effective only for targets with shell ρR's less than 180 mg cm^{-2}, since these fusion products are ranged out at higher ρR's. Second, the technique requires that the nuclear bang time fall within or near the end of the laser pulse, so that fusion products are born with a measurable energy upshift due to the target potential, which is not the case for typical cryogenic implosions. Finally, while direct measurements of the potential using fast voltage probes are feasible, there is no guarantee that the probe would not perturb the electrical circuit and result in an erroneous measurement.

To gain insight into the potential decay dynamics of spherical ICF implosions, we present a circuit model based on empirical circuit elements that are obtained from recently published studies [7, 9]. In these studies, comprehensive measurements of fast ions on OMEGA were used to infer the voltage-dependent capacitance associated with the electrostatic field surrounding the target. In addition, measurements of the current profiles of OMEGA target stalks were used to estimate the time-dependent inductance and resistance of the stalks. This discharging model can be used to predict potential decay times, and can be incorporated into hydrodynamic codes that are used to model ICF implosions. The hydrodynamic code LILAC [10], for instance, assumes at present that the target potential is large for all time and that all hot electrons are trapped within the target, resulting in an overestimate of target preheat [11].

In addition to providing predictive capability for OMEGA implosions, the model can be used to study target discharging in the absence of target stalks, a scenario encountered in present inertial fusion energy (IFE) concepts [12]. Finally, the methods employed in developing this model can be ultimately extended to the National Ignition Facility (NIF) and applied to other fields within the broader ICF community (e.g. Z-pinch circuit models).

This paper is organized as follows: section 2 presents an overview of the target discharging model. In section 3, the model parameters are determined using previous spectral and radiographic measurements, followed by a numerical solution and discussion of the potential decay dynamics in section 4. Section 5 discusses the implications of the model in the context of IFE, and section 6 summarizes our findings and discusses limitations of the model.

2. Model overview

The capsule discharging model is developed by first considering the acceleration of fast ions from the coronal plasma toward the target chamber wall. These ions, with maximum energies of ∼1 MeV and yields of 10^{13}–10^{14}, deplete the initial positive charge on the target that was created by escaping hot electrons. These ions thus expand together with the hot electrons (temperature of T_h) with a characteristic velocity given by the hot-electron sound speed ($c_h \equiv \sqrt{T_h/m_i}$), reducing the target potential (the strength of the sheath fields surrounding the target) as the target shell is imploding. This hot-electron and fast-ion expansion front is the sheath boundary ($R(t) \sim c_h t$) indicated in figure 1(*a*). Outside this boundary, the fields are screened and the potential is zero. The structure of the sheath is discussed further in section 3. The decay of the potential is thus captured by a lumped circuit element model consisting of a capacitor (C_T) discharging through a resistor (R_I, see figure 1). The capacitor

represents the space charge across the sheath surrounding the target, while the parallel time-dependent resistor allows for a flow of direct current across the sheath in the form of fast ions. The stalk is composed of segments of silicon carbide (70 μm diameter, 1 cm long) and boron (140 μm diameter, 1 cm long) and connects the target to the electrically grounded chamber. It allows the flow of current to and from the target and is modeled using a series resistor–inductor combination (figure 1). It has been shown recently that currents flow along a thin outer layer of the stalk that is ionized early on in the implosion (by the large potential across the stalk) [9]. This annulus has been observed to be several tens of micrometers thick, which is comparable to the skin depth of the stalk ($\delta \sim 50\,\mu$m) for the fast voltage pulses considered here. This thin layer of the stalk explodes outward as it carries current, resulting in an inductance that decreases with time, whereas the core of the stalk remains intact even after the implosion and does not carry current.

Given this circuit model, the goal is to determine the decay time of the system, or equivalently, the voltage on the capacitor (the target potential) as a function of time. Although the model itself can be applied to a wide range of targets, the parameters are empirically derived in the following section and have limited scope. We restrict the discussion to either warm or cryogenic spherical targets consisting of $\gtrsim$10–μm thick plastic or glass shells irradiated on OMEGA with intensities of (4–10) $\times\ 10^{14}\,\mathrm{W\,cm^{-2}}$.

We assume that the target voltage rise time is fast relative to the decay time ($\tau_\mathrm{r} \ll \tau_\mathrm{d}$). The voltage rise time is characterized by the time it takes for the fastest electrons of the hot-electron population ($\gtrsim$50 keV) [13] to traverse and escape the target ($\sim$1 mm diameter), which is on the order of $\sim$10 ps. Exact calculation of τ_r is difficult because hot electrons are produced continuously and the voltage peaks when the source of hot electrons equals the charge sinks (fast-ion acceleration and stalk currents).

For the OMEGA implosions considered here the onset and duration of hot-electron production increases with increasing laser intensity [6]. At an intensity of $4 \times 10^{14}\,\mathrm{W\,cm^{-2}}$, onset occurs $\sim$400 ps into the flat-top portion of the laser drive regardless of the pulse shape (i.e. pickets preceding the main drive have little to no effect). Similarly, at an intensity of $1 \times 10^{15}\,\mathrm{W\,cm^{-2}}$, onset of hot-electron production occurs near the start of the main drive. In both cases, hot-electron production lasts for the rest of the laser drive. These conclusions were drawn by observing the time-resolved $3\omega/2$ emission [6] associated with the TPD instability and the hard x-ray emission that comes from electrons stopping on the shell [13]. We thus expect the target potential to reach its peak value tens of picoseconds after the onset of hot-electron production. The empirical relationship between peak target voltage and laser intensity is given by [7]

$$V_0 = 0.12 I_{14} - 0.4\,\mathrm{MV}, \tag{1}$$

where V_0 is in megavolts and I_{14} is the on-target laser intensity in units of $10^{14}\,\mathrm{W\,cm^{-2}}$ [5, 7].

The decay time of the potential depends on the magnitude of currents in the stalk and how quickly fast ions are accelerated from the target to deplete the space charge. As shown in this paper and first measured on OMEGA by Hicks *et al* [5] the potential falls soon after the laser turns off resulting in a decay time of $\lesssim$1 ns. We thus focus on modeling the decay time, and the initial conditions of our model are $V_{\mathrm{T}|_{t=0}} = V_0$ and $\mathrm{d}V_\mathrm{T}/\mathrm{d}t|_{t=0} = 0$, where $t = 0$ corresponds to a few tens of ps after the onset of hot-electron production.

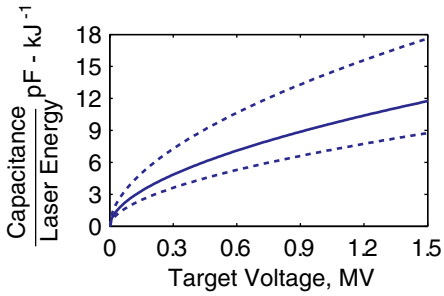

Figure 2. Target capacitance (C_T), in units of picofarads per kilojoule of laser energy, as a function of the instantaneous target voltage. The dashed curves indicate the absolute uncertainty of the measured capacitance (see [7]).

This model is only valid for positive target voltages. For negative target voltages, the model no longer portrays the underlying physical picture. Once the target voltage crosses zero, the space charge no longer exists and current cannot flow in the reverse direction (the hot electrons and fast ions expand adiabatically). In this sense the capacitor–resistor branch of the target behaves like a diode. In the following analysis, we constrain the target voltage to $V_\mathrm{T} > 0$.

3. Empirical circuit parameters

The values of the lumped circuit elements have been determined empirically, using charged-particle spectroscopy [14] and monoenergetic charged-particle radiography [15]. Some of these measured parameters will be swept within their experimental uncertainties to obtain the best agreement with the measured temporal evolution of the target potential, as discussed in section 4. In each of the following subsections, we use the results of [7, 9] to extract parameters relevant to the circuit model.

3.1. Target capacitance

The capacitor in the model scales nonlinearly with the instantaneous target voltage and linearly with laser energy as described by [7]:

$$C_\mathrm{T} = C_0 V_\mathrm{MV}^{\alpha} E_\mathrm{L}\ pF, \tag{2}$$

where V_MV is the instantaneous target voltage in megavolts, E_L is the incident laser energy in kilojoules, and the constants are $C_0 = 9.4^{+4.7}_{-2.4}$ and $\alpha = 0.55 \pm 0.03$. The capacitance is implicitly time-dependent since its value changes with the voltage on the target (shown in figure 2(*a*)). It was inferred from time-integrated measurements of fast-ion energy spectra using several OMEGA shots. For each shot, the peak target voltage was inferred from the maximum proton energy, and the amount of energy discharged by the capacitor was

determined from time-integrated measurements of the fast-ion energy spectra. Each shot thus measured the total energy stored in the electrostatic fields surrounding the target (the capacitor) as a function of initial voltage. These measurements were performed for different target and laser configurations, culminating in a dataset with a wide range of peak-voltage values that were then converted to a capacitance as a function of *instantaneous* voltage. The capacitance was found to be independent of the target material (CD, CH or SiO_2), shell thickness or laser parameters (intensity and pulse duration, but not independent of energy).

Equation (2) assumes that all of the charge leaves the target in the form of fast ions, which is not strictly true. The total charge leaving the capacitor includes current through the stalk, which is neglected in this formulation. This additional term is estimated in section 3.3 and later added to (2).

3.2. Charge-leakage resistance

The resistor R_I allows the flow of fast-ion current away from the target for a given instantaneous target voltage. This resistance can be written as a function of the voltage across the expanding sheath (the target potential), the current density (J) and the surface area (A) of the expanding fast ion and hot-electron front:

$$R_I = \frac{V_T}{J\ A}. \tag{3}$$

The current density is defined as $J \equiv e(n_i v_i - n_e v_e)$, where e is the elementary charge and $n_{i(e)}$ and $v_{i(e)}$ are the ion (electron) density and velocity, respectively. The surface area of the expanding sheath front is $A = 4\pi r_f(t)^2$, where $r_f(t)$ is the time-dependent radius of the front. The voltage in (3) will be solved for self-consistently in section 4, while the current can be estimated using a fluid model and Poisson's equation as follows.

Consider the density profiles of hot electrons and fast ions shown in figure 3. Such profiles have been previously simulated by authors that treated the expansion of cold ions ($T_i \approx 0$) by a hot-electron population [16, 17]. The hot-electron density follows the ion density until the local density scale length becomes comparable to the local Debye length, as indicated by the dashed line at $r = r_q$. For $r > r_q$, quasineutrality is violated and a sheath is formed over a few Debye lengths ($\lambda_{D,h} \sim 0.1\,\mu$m). The target voltage drops over both the quasineutral and sheath regions as indicated in figure 3. The current flows in the sheath region and this is understood as follows. As electrons cool, they give energy to the ions and fall behind (λ_D decreases). The density of electrons at r_f increases in time and this amounts to a current. To compute the current, we take the flow velocity of the ions and electrons to be equal ($v_i \approx v_e$) and estimate this velocity using the flow velocity evaluated at r_q. Thus, $J \approx e(n_i - n_e)v_q$, and we then estimate $n_i - n_e$ using Poisson's equation, $\epsilon_0 \nabla^2 \phi_s \approx 3\phi_s/\lambda_{D,q}^2 = -e(n_i - n_e)$, where $\phi_s = V_T - \phi_q$ is the potential in the sheath region and $\lambda_{D,q}$ is the Debye length evaluated at r_q. We furthermore estimate the area using $r_q(t)$ in place of $r_f(t)$, which is a reasonable approximation since $r_f(t) = r_q(t) + \mathcal{O}(\lambda_D)$, and $r_q(t) \gg \mathcal{O}(\lambda_D)$. The resistance is then given by

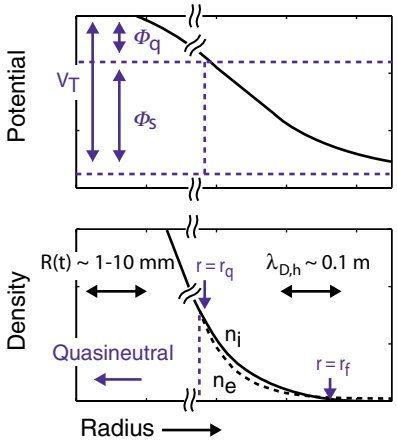

Figure 3. Structure of the ion front, including the electron and ion densities and potential. The target potential (V_T) is the sum of the voltage drop across the quasineutral region (ϕ_q) and across the sheath (ϕ_s).

$$R_I = \frac{V_T}{12\pi\epsilon_0 v_q r_q(t)^2 (V_T - \phi_q)/\lambda_{D,q}^2}. \tag{4}$$

To proceed, we require solutions for the hydrodynamic variables (density, temperature, velocity and potential) and knowledge of the position r_q at all times, which are described next.

In a 1D spherical geometry, the potential (ϕ), temperature (T_h), density (n), velocity (v) and characteristic size (R) of the quasineutral region are given by [16, 17]

$$\phi(r,t) = T_h(t)[r/R(t)]^2 \tag{5}$$

$$T_h(t) = T_{h,0}[R_0/R(t)]^2 \tag{6}$$

$$n(r,t) = n_0\,[R_0/R(t)]^3 \exp[-(r/R(t))^2] \tag{7}$$

$$v(r,t) = (2\ q\ r\ t\ T_{h,0})/[m_i(R_0^2 + 2c_{h,0}^2 t^2)]. \tag{8}$$

$$R(t) = (R_0^2 + 2c_{h,0}^2 t^2)^{1/2}. \tag{9}$$

Here, n_0 is the initial density of the fast ions, R_0 is the corona edge when hot electrons are produced, $c_{h,0} \equiv (T_{h,0}/m_i)^{1/2}$ is the initial hot sound speed and $R(t)$ is the radius where the fast-ion density profile has fallen to n_0/e (hence $R(t) < r_q(t)$). In the derivation of equations (5)–(9), it is assumed that the electrons expand adiabatically. Hot-electron production is a complex process involving both energy loss and gain and it is not entirely obvious that the adiabatic assumption is valid. Electrons that are trapped within the target reflux and lose energy to the unablated part of the shell (preheat). They also gain energy from electron-plasma waves (generated by the TPD instability at the quarter-critical surface) as they pass through the corona. Furthermore, electrons in the sheath region (figure 3) can lose energy and become trapped, while trapped electrons that gain sufficient energy from the corona can escape and drive ion acceleration. Simulations by Myatt *et al* [18] demonstrate that this process results in a Maxwellian

distribution of hot electrons and that the net effect of trapping the electrons is to increase their temperature. This suggests that the time dependence of the potential plays a role in prescribing the amount of refluxing (and hence reheating) of the trapped electrons. The fact that refluxing of hot electrons is important can be readily seen by comparing the refluxing time with the decay time of the potential. We will show in section 4 that the latter is on the order of 1 ns, while refluxing time of a hot electron is $R(t)/v_e \lesssim 100$ ps. Another consequence of refluxing is that the hot-electron temperature is uniform in space and that the adiabatic index (γ) is 5/3 since scattering in the shell relaxes the distribution to a Maxwellian over three degrees of freedom. The results of Myatt *et al* also demonstrate that the adiabatic assumption is not strictly valid. Use of this assumption in our model is justified for two reasons. First, the hot-electron temperature used in these calculations is the measured time-averaged temperature that implicitly accounts for the aforementioned sources and sinks in our problem. The time-averaged hot-electron temperature was inferred from the hard x-ray spectrum produced when electrons stop on the shell and was found to vary linearly from 25 to 50 keV for incident laser intensities of (4–10) $\times$ 10^{14} W cm^{-2} [13][1]. Second, a study was conducted to examine the sensitivity of the circuit model to uncertainties in each of the circuit elements [19]. It was found that our circuit model is insensitive to a factor of ~3 changes in the resistance and hence comparable uncertainties in the hot-electron temperature.

Next, we find $r_q(t)$ by setting the local density scale length equal to the local Debye length ($\lambda_{D,q}\nabla n_q/n_q = 1$). Making use of equations (5)–(9), we obtain a transcendental equation for $r_q(t)$:

$$r_q(t) = \sqrt{2}R(t)\left[\ln\left(\frac{R_0^{5/2}}{2r_q(t)\lambda_{D,0}R(t)^{1/2}}\right)\right]^{1/2}, \qquad (10)$$

where $\lambda_{D,0}$ is the initial Debye length. This equation is solved numerically for a given time value. Equations (5)–(10) are then evaluated at r_q and combined with (4) to obtain the resistance:

$$R_I = V_T \times \frac{m_i R_0^4}{384\sqrt{2}\pi\epsilon_0 e t T_{h,0}\left(R_0^2 + 2c_{h,0}^2 t^2\right)^{3/2}\left(\phi_q - V_T\right)} \times \ln\left[2r_q(t)\left(R_0^2 + 2c_{h,0}^2 t^2\right)^{1/4}\lambda_{D,0}/R_0^{5/2}\right]^{-5/2}. \qquad (11)$$

The resistance depends on the initial values of the hot-electron temperature, size of the sheath and the fast-ion density. The temperature is routinely measured and the initial sheath radius is estimated ($R_0 \sim 1$ mm) based on hydrodynamic simulations. The initial fast-ion density is just N_i/V_i, where $N_i \equiv C_T V_0/e$ is the number of ions and V_i is the volume they occupy. Initially, these ions will be confined to a spherical shell around R_0 with a characteristic shell thickness of $\lambda_{D,0} \sim 1\,\mu$m. The volume was left as a fit parameter but was constrained to scale with the Debye length for different laser intensities and hence hot-electron temperatures ($V_i \propto \lambda_{D,0} + \mathcal{O}(\lambda^2)$ for the case of $\lambda_{D,0} \ll R_0$). The fit parameter was determined by comparing the model against Hicks' measurement. As discussed in section 4, good agreement was obtained for $R_0 \sim 1.5$ mm and $n_0 \sim 10^{14}$–10^{17} cm^{-3}. The scaling of n_0 with Debye length and capacitance produced reasonable results for other cases.

3.3. Stalk inductance and resistance

The resistance and inductance of target stalks have been previously inferred using time-gated proton radiography [9]. This technique [15] uses a monoenergetic-proton backlighter, driven by several OMEGA beams, to infer path-integrated magnetic and electric field strengths of a subject that is driven by a separate set of OMEGA beams. In this case, the subjects were the silicon carbide and boron stalks that supported the imploding ICF capsules. The relative timing between the laser beams that drive the proton backlighter and the target was varied to sample the stalk at different times. Using this technique, radiographs containing information about the electric and magnetic fields surrounding the stalk were produced at different times. The temporal evolution of the stalk plasma and current were thus studied over several shots for a peak target potential of ~100 kV (figure 4).

Simulations indicated that a current flowing in a cylindrical annulus surrounding the stalk reproduced the radiographs and that portions of the annulus were charged [9]. The time-dependent inner and outer radii of the annulus ($R_i \sim$ 70–500 μm and $R_o \sim$ 110–1100 μm) and hence the expansion speed of the annuli were also inferred. The expansion speed is consistent with either electrostatic acceleration (e.g. coulomb explosion of the stalk) or the thermal expansion of a 500 eV stalk plasma. Initially, the ionized outer layer of the stalk is cold ($T_s \sim 10$ eV) and ohmic heating is not large enough to heat this plasma to 500 eV. In fact, a self-consistent heat transfer calculation with an ohmic source (neglecting expansion, convection and diffusion which only cool the stalk plasma) shows that the temperature increases by about a factor 2 over 1 ns). We thus conclude that the stalk blows apart due to electrostatic forces rather than ohmic heating and subsequent thermal expansion[2]. Given this result, we expect the stalk to expand slightly faster for larger drive voltages (target potentials). As a result, the time-dependent annuli from [9] were scaled for different initial voltages (R_i and R_o scale with the expansion velocity that is proportional to $\sqrt{V}$) and then used to calculate the inductance. The inductance [20] and resistance of a wire with length l_s, inner radius R_i and outer radius R_o are given by

$$L_S = \frac{\mu_0}{2\pi}R_o\left[\frac{l_s}{R_o}\ln\left(l_s/R_o + \sqrt{l_s^2/{R_o}^2 + 1}\right) - \sqrt{l_s^2/{R_o}^2 + 1} + 1\right] \qquad (12)$$

$$R_S = \frac{\eta\, l_s}{\pi R_o^2[1 - (R_i/R_o)^2]}, \qquad (13)$$

[1] An analytical error was identified in the analysis used in [13] and when corrected the hot-electron temperatures are 40% lower (Source: private communication with Stoeckl).

[2] The authors previously published an incorrect time constant (L_S/R_S) using $T_s \sim 500$ eV by assuming the expansion of stalk plasma was thermal-driven [9].

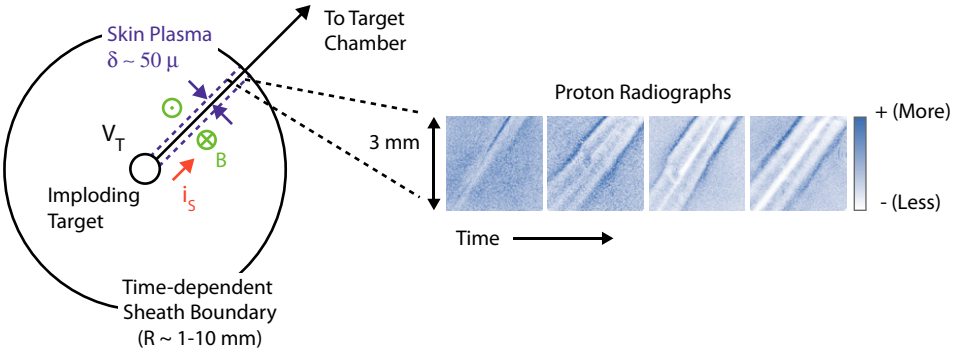

Figure 4. Schematic of the target support stalk, skin plasma and the sheath boundary (left). The target potential generates a skin plasma around the stalk and drives an ohmic current through it. The magnetic fields generated by this current deflect protons from a backlighter (not shown) which can be detected and imaged at various times (right). These images of proton fluence variation contain information about the geometry of the current annulus and illustrate the temporal evolution of the skin plasma surrounding the stalk. In particular, the field structures expand away from the stalk center as the plasma evolves. See [9] for a detailed analysis and discussion of these proton radiographs.

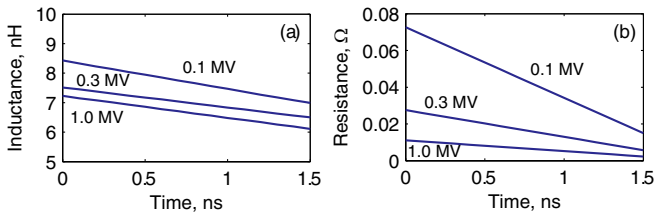

Figure 5. Stalk (a) inductance (L_S) and (b) resistance (R_S) as a function of time for several values of peak target potential. For these plots, $t = 0$ corresponds to the time when the voltage has reached its peak value, at which point the skin plasma surrounding the stalk is well-established. The current carrying stalk plasma expands in time, resulting in larger plasma cross section and hence lower inductance and resistance values. In addition, larger peak target potentials cause the stalk to blow apart faster, resulting in lower inductance and resistance for larger peak potentials. The values shown here are for an effective stalk length of 2 cm.

where η is the Spitzer resistivity ($\propto T_s^{-3/2}$ with $T_s \sim 10$ eV). The time-dependent inductance and resistance curves for these stalks are shown in figure 5 for several initial drive voltages. The precision of the inferred annuli and hence the inductance and resistance are high ($\pm 50\,\mu$m). The systematic uncertainty arises from the fact that the stalk length that contributes to these circuit parameters is not well known. The portion of the stalk that sees an electric field and hence carries current is limited to the region within the sheath boundary. As discussed in section 3.2, the sheath boundary is the fast-ion and hot-electron expansion front that expands at the hot-electron sound speed. We estimate that the boundary starts at the target radius and expands out to ~1–2 cm. For simplicity, we use a time-averaged effective stalk length in subsequent calculations, and scale the length with the hot-electron sound speed and with laser intensity. It will be shown in section 4 that agreement was obtained with experimental data for a time-averaged effective stalk length of ~2 cm, as determined by fitting the model to experimental data.

Finally, these measurements were used to correct the capacitance (2). For targets with a peak voltage of ~100 kV, ($I_L = 4 \times 10^{14}$ W cm^{-2}), the amount of charge that leaves the stalk is measured to be comparable to the amount of charge expelled from the target in the form of fast ions. Since measurements for higher laser intensities and hence larger driving voltage are not available, we take the amount of charge leaving the stalk to scale with the initial voltage, since a larger voltage will to first order drive a proportionally larger current.

4. Voltage decay time

The dynamics of the voltage decay are described by a nonlinear differential equation. The governing equations are derived here in the time-domain and then solved numerically. The charge on the capacitor (Q_T) depletes over time according to

$$\frac{dQ_T}{dt} = -(i_A + i_S), \tag{14}$$

where the fast-ion current (i_A) and the stalk current (i_S) are given by

$$i_A = V_T/R_I \tag{15}$$

$$i_S = \left(V_T - L_S\frac{di_S}{dt}\right)/R_S, \tag{16}$$

where R_S and L_S are the time-dependent resistance and inductance of the stalk, and where R_I represents the time-dependent parallel leakage path that allows for fast-ion acceleration. Equation (16) implies that the inductance varies slowly compared with the decay time [$L_s(dL_s/dt)^{-1} \ll \tau_d$], which is evident by comparing a ~1 ns decay time to the inductance curves in figure 5(a). Combining Equations (14)–(16), together with the continuity equation ($i_C = i_A + i_S$) results in the following differential equation for the charge on the capacitor:

$$\frac{d^2Q_T}{dt^2} + \frac{R_S}{L_S}\frac{dQ_T}{dt} + \frac{d}{dt}\left(\frac{Q_T}{R_IC_T}\right) + \frac{Q_T}{L_SC_T}\left(\frac{R_S + R_I}{R_I}\right) = 0. \tag{17}$$

No assumptions have been made at this point regarding the nonlinearity or time-dependence of the circuit elements, with the exception of the inductor, which is taken to vary slowly compared with the decay time. It is evident from inspection of (17) that the stalk inductance and resistance contribute a time constant to the system (L_S/R_S), while the target capacitance

and resistance ($R_I C_T$) contribute another. Furthermore, the charge-leakage resistance modifies the bandwidth of the system. Next, we incorporate the relation between capacitance and charge ($Q_T = C_T V_T$) and use the empirical expression for capacitance ($C_T \sim V_T^{\alpha}$) to obtain a differential equation for the voltage on the capacitor:

$$\frac{d^2 V_T}{dt^2} + \frac{\alpha}{V_T}\left(\frac{dV_T}{dt}\right)^2 + \left[\frac{R_S}{L_S} + \frac{1}{R_I C_T\,(1+\alpha)}\right]\frac{dV_T}{dt} + \left[\frac{1}{(1+\alpha)\,L_S C_T}\left(\frac{R_I + R_S}{R_I} - \frac{L_S}{R_I^2}\frac{dR_I}{dt}\right)\right] V_T = 0. \quad (18)$$

For a linear capacitor, the dynamics of the charge describe the behavior of the voltage. It is clear from (18) that the nonlinearity of the capacitance adds a second-order damping term (second term) and modifies the $R_I C_T$ time constant and bandwidth by a scalar factor.

The numerical solution to (18) was found using the values discussed in section 3. In particular, the stalk length and initial ion density were swept to match the constraints on total decay time and the shape of the experimental measurements, respectively. The experiments utilized 900 μm diameter thin-glass shells irradiated with 1 ns square laser pulses with a total energy of 26 kJ resulting in on-target laser intensities of 9×10^{14} W cm^{-2} [4], and a peak voltage of 660 kV [7]. The results of the numerical calculation are shown in figure 6(a) (solid curve) alongside the measured values and the square laser pulse. The absolute uncertainty of the voltage and time error bars of each data point are also shown, along with an estimate of what the voltage rise might look like. Agreement was obtained for an effective stalk length of ~2 cm (reduced $\chi^2 = 2$).

The effective stalk length was constrained by the measured data and by the total decay time. The target cannot begin charging before hot-electron production starts, as indicated by the arrows in figure 6, and we expect the rise time to be ~10–100 ps. Further increase in the effective stalk length increases the inductance of the system, decreases the current flow through the stalk and hence increases the decay time. This leaves little time for the voltage to rise and violates that constraint. The peak magnitude of current flowing through the stalk for a laser intensity of 4×10^{14} W cm^{-2} is comparable to measurements by Manuel *et al* ($i_s \sim 7$ kA). In addition, the total charge flowing through the resistor R_I is consistent with the total measured charge of fast ions emitted by the target (see [7]). At higher intensities, the model predicts 1.5–2 times more charge flowing through R_I than is observed. This shortcoming is reasonable given the lack of stalk measurements at higher intensities, and hence the poor estimate of the capacitance as discussed at the end of section 3.3.

Figure 6(b) shows the relative magnitudes of the terms in (18). The bandwidth term is the dominant term for the first several hundred ps after which the $R_I C_T$ term takes over, while the nonlinear and stalk damping terms of (18) are negligible. The circuit is thus an under damped system and the decay shown in figure 6(a) is a quarter-cycle of an oscillation for the first few hundred ps. The rest is damped by the $R_I C_T$ term, which corresponds to damping by fast-ion acceleration. It is worth noting that the shape of Hicks' data alone also

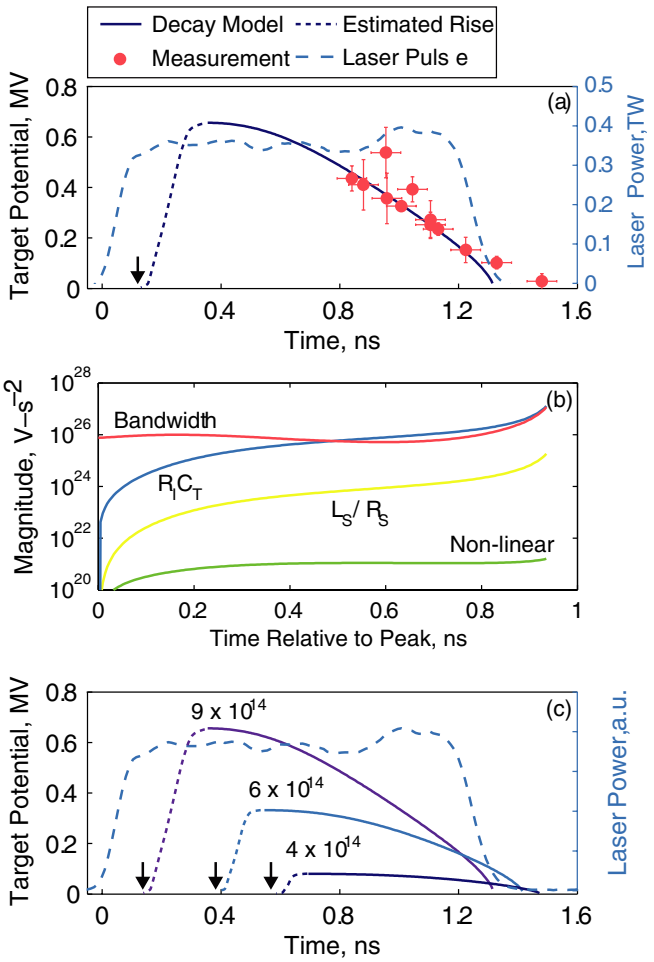

Figure 6. (a) The modeled decay of the target voltage (solid curve) is shown together with measurements by Hicks for a laser energy of 26 kJ and intensity of 9×10^{14} W cm^{-2}. Also shown are the laser pulse shape used in the experiments (dashed curve) and the target voltage rise. (b) Magnitude of the damping and bandwidth terms of (17). (c) Voltage decay curves for 860 μm diameter targets irradiated with a 1 ns pulse with laser energies of 12, 18 and 26 kJ, corresponding to on-target intensities of 4, 6 and 9×10^{14} W cm^{-2}. Arrows indicate the onset of hot-electron production.

suggests that both the stalk and fast-ion current must discharge the target. If only the $R_I C_T$ term were dominant, the shape of $V_T(t)$ would be concave (e.g. decaying exponential) and does not match the measurement. Similarly, if only the bandwidth term were dominant, the shape of $V_T(t)$ would be convex (e.g. sinusoidal). The competition between these two terms flattens out $V_T(t)$ and agrees better with Hicks' measurement. This was verified by heuristically changing circuit parameters to make one term more dominant than the other.

The voltage decay time decreases with decreasing laser intensity (see figure 6(c)). For lower laser intensities, the onset of hot-electron production occurs later relative to the start of the pulse [6]. Decay curves are shown in figure 6(c) for an 860 μm diameter target irradiated with laser energies of 12, 18 and 26 kJ, corresponding to on-target intensities of 4, 6 and 9×10^{14} W cm^{-2}. These curves have been time-shifted to account for onset of hot-electron production and show that the voltage goes to zero shortly after the end of the laser

Table 1. Parameters used in the calculation of the voltage decay curves of figure 6(*c*), including the laser intensity (I_L), laser energy (E_L), measured hot-electron temperature ($T_{h,0}$), measured peak voltage (V_0), modeled stalk length (l_s) and initial ion density (n_0). Model predictions for the peak stalk current ($i_{s,p}$), ratio of the number of predicted to measured fast ions ($N_{i,p}/N_{i,m}$) and decay time (τ_f) are also shown.

I_L (W cm^{-2})	E_L (kJ)	$T_{h,0}$ (keV)	V_0 (MV)	l_s (cm)	n_0 (cm^{-3})	$i_{s,p}$ (kA)	$N_{i,p}/N_{i,m}$	τ_f (ns)
4×10^{14}	12	24	0.08	1.46	2.7×10^{14}	6	1.25	0.78
6×10^{14}	18	32	0.33	1.72	5.9×10^{16}	29	1.72	0.87
9×10^{14}	26	44	0.66	2.00	6.6×10^{17}	55	2.11	0.96

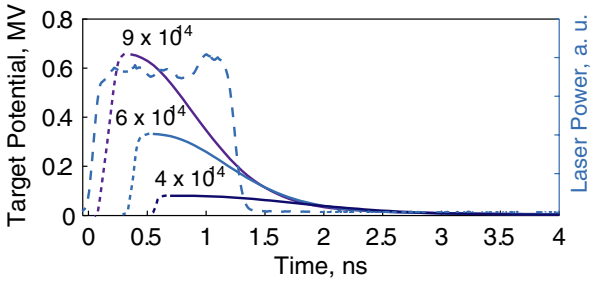

Figure 7. Voltage decay curves for (hypothetical) OMEGA targets without stalks. These curves are for 860 μm diameter targets irradiated with a 1 ns pulse with laser energies of 12, 18 and 26 kJ, corresponding to intensities of 4, 6 and 9×10^{14} W cm^{-2}.

pulse. The parameters used in the calculation of figure 6(*c*) are summarized in table 1.

5. Implications for IFE

Since IFE requires the implosion of targets with high-repetition rates (~10 Hz) [12], the use of a support stalk is impractical. Current designs make use of targets without supporting stalk fibers, which are launched into a chamber at which point they are tracked and subsequently shot [21]. Since the stalk plays an important role in discharging the target, we expect IFE targets to discharge over a longer period of time.

The absence of a stalk amounts to setting (16) to zero, preventing current flow through the stalk. This is equivalent to analyzing (18) in the limit $L_S \to 0$ and $R_S \to \infty$, which results in

$$\frac{dV_T}{dt} + \left[\frac{1}{(1+\alpha)\ R_I C_T}\right] V_T = 0. \tag{19}$$

This equation is solved numerically since R_I is a nontrivial function of time. The results are shown in figure 7 for an 860 μm diameter target irradiated with laser energies of 12, 18 and 26 kJ (corresponding on-target laser intensities of 4, 6 and 9×10^{14} W cm^{-2}). The voltage decay time increases with decreasing laser intensity, but the dependence is weak. The absolute time when the potential goes to zero varies significantly because the onset of hot-electron production varies with intensity. The weak dependence of the decay time on laser parameters can be understood as follows. For a lower laser intensity and hence a lower peak voltage, the capacitance is smaller and there is less charge to remove. However, the resistance is roughly proportionally larger because there are less charge carriers and this results in a weakly varying $R_I C_T$ time constant. This is most easily seen from the analytic expression for ϕ_q. Although this expression does not include charge separation effects, it gives a feel for scaling of the potential decay time. The time it takes for the voltage to drop to $1/e$ of its initial value (τ_{ns}) can be found by inverting (5):

$$\tau_{ns} \sim R_0/(T_{h,0})^{1/2}. \tag{20}$$

Since the geometry is fixed for OMEGA targets ($R_0 \sim 860\,\mu$m) the decay time decreases with increasing laser intensity, albeit weakly, as observed in figure 7. The scaling of τ_{ns} with R_0 is confirmed by our numerical solution to (19), although it is not readily apparent from the expressions for R_I and C_T.

Figure 7 illustrates the effect of removing the stalk for OMEGA targets, but current designs for IFE-scale targets (i.e. direct-drive ignition-scale targets) will have longer discharge curves. IFE targets are larger than those used at OMEGA by a factor of 2–3. They are irradiated at comparable on-target laser intensities (~7×10^{14} W cm^{-2}) but with higher total laser energy (~2 MJ). Under these conditions, the hot-electron temperature is ~2 times higher for a given intensity and hot-electron production is driven to saturation at $\lesssim$1% of the laser energy [22]. Since the discharge time scales roughly with the geometry and hot-electron temperature for targets without stalks, we expect the decay times for IFE-scale targets to be roughly two times longer than the curves shown in figure 7. Detailed studies can be carried out once the hot-electron production for these targets, and hence the capacitance has been thoroughly characterized.

A longer decay time in the absence of a stalk implies that preheat in these targets will be higher than in stalk-mounted targets, which depends on the detailed dynamics of trapped electrons passing through the target shell. This will be addressed in the future using simulations that utilize these voltage decay curves. The role of the stalk is thus significant but the underlying physics is subtle. The L_S/R_S time constant alone does not play a large role since it is longer than the decay time. However, it is evident that charging the inductor (stalk) with current (as represented by the bandwidth term in (18)) results in faster expulsion of charge from the target.

6. Conclusion

In summary, we have presented a circuit model that describes the voltage decay dynamics of spherical, stalk-mounted targets shot on OMEGA. The circuit elements of the model were determined from previous spectral measurements of fast ions and radiography of target stalks. This model captures the essential physics of the decay dynamics and provides valuable insight into the role of the target support stalk in the discharging process.

Some of the circuit elements are approximate and require refinement for detailed quantitative studies. Measurements of stalk characteristics at higher laser intensities and hence higher drive voltage are required to correct the capacitance and to verify the physics of stalk plasma evolution in this regime.

Time-resolved measurements of the fast-ion current can also be used to further validate the resistance (R_l) formalism employed here. Finally, our model assumes that electrons are generated in a burst (that the capacitor is initially charged to a voltage and subsequently discharges), which is an approximation since electrons are produced over a few hundred picoseconds or an appreciable fraction of the total decay time. This model can thus be refined by incorporating a detailed time-dependent electron source and additional charge sinks such as electron stopping in the shell.

It has been shown on the basis of this model that the target stalk plays a significant role in the voltage decay dynamics. In particular, it was shown that the voltage decay time depends weakly on the laser intensity and that it is longer for targets without stalks.

Acknowledgments

This work was supported by the National Laser User's Facility (DOE Award No DE-NA0000877), and was completed as part of the author's PhD Thesis.

References

[1] Pearlman J S and Dahlbacka G H 1977 Charge separation and target voltages in laser-produced plasmas *Appl. Phys. Lett.* **31** 414–17

[2] Benjamin R F, McCall G H and Ehler A W 1979 Measurement of return current in a laser-produced plasma *Phys. Rev. Lett.* **42** 890–3

[3] Boehly T R *et al* 1997 Initial performance results of the OMEGA laser system *Opt. Commun.* **133** 495–506

[4] Hicks D G *et al* 2001 Observations of fast protons above 1 MeV produced in direct-drive laser-fusion experiments *Phys. Plasmas* **8** 606–10

[5] Hicks D G *et al* 2000 Charged-particle acceleration and energy loss in laser-produced plasmas *Phys. Plasmas* **7** 5106–17

[6] Seka W, Edgell D H, Myatt J F, Maximov A V, Short R W, Goncharov V N and Baldis H A 2009 Two-plasmon-decay instability in direct-drive inertial confinement fusion experiments *Phys. Plasmas* **16** 052701

[7] Sinenian N *et al* 2012 Total energy loss to fast ablator-ions and target capacitance of direct-drive implosions on OMEGA *Appl. Phys. Lett.* **101** 114102

[8] Goncharov V N *et al* 2008 Performance of direct-drive cryogenic targets on OMEGA *Phys. Plasmas* **15** 056310

[9] Manuel M J-E, Sinenian N, Séguin F H, Li C K, Frenje J A, Rinderknecht H G, Casey D T, Zylstra A B, Petrasso R D and Beg F N 2012 Mapping return currents in laser-generated z-pinch plasmas using proton deflectometry *Appl. Phys. Lett.* **100** 203505

[10] Delettrez J, Epstein R, Richardson M C, Jaanimagi P A and Henke B L 1987 Effect of laser illumination nonuniformity on the analysis of time-resolved x-ray measurements in uv spherical transport experiments *Phys. Rev.* A **36** 3926–34

[11] Delettrez J 2013 private communication

[12] Moses E I 2009 Ignition on the National Ignition Facility: a path towards inertial fusion energy *Nucl. Fusion* **49** 104022

[13] Stoeckl C *et al* 2003 Multibeam effects on fast-electron generation from two-plasmon-decay instability *Phys. Rev. Lett.* **90** 235002

[14] Séguin F H *et al* 2003 Spectrometry of charged particles from inertial-confinement-fusion plasmas *Rev. Sci. Instrum.* **74** 975–95

[15] Manuel M J-E, Zylstra A B, Rinderknecht H G, Casey D T, Rosenberg M J, Sinenian N, Li C K, Frenje J A, Séguin F H and Petrasso R D 2012 Source characterization and modeling development for monoenergetic-proton radiography experiments on OMEGA *Rev. Sci. Instrum.* **83** 063506

[16] Mora P 2005 Collisionless expansion of a gaussian plasma into a vacuum *Phys. Plasmas* **12** 112102

[17] Murakami M and Basko M M 2006 Self-similar expansion of finite-size non-quasi-neutral plasmas into vacuum: relation to the problem of ion acceleration *Phys. Plasmas* **13** 012105

[18] Myatt J F, Zhang J, Delettrez J A, Maximov A V, Short R W, Seka W, Edgell D H, DuBois D F, Russell D A and Vu H X 2012 The dynamics of hot-electron heating in direct-drive-implosion experiments caused by two-plasmon-decay instability *Phys. Plasmas* **19** 022707

[19] Nareg Sinenian 2013 Fast-ion spectrometry of ICF implosions and laser-foil experiments at the Omega and MTW laser facilities *PhD Thesis* Massachusetts Institute of Technology

[20] Rosa Ed B 1908 *The Self and Mutual-inductance of Linear Conductors* vol 4 (Washington, DC: National Bureau of Standards)

[21] Petzoldt R W, Goodin D T, Valmianski E, Carlson L C, Stromsoe J D and Hares J 2009 Target steering and electrostatic acceleration for IFE *23rd IEEE/NPSS Symp. on Fusion Engineering, 2009. SOFE 2009 (San Diego, June 2009)* pp 1–4

[22] Froula D H *et al* 2012 Saturation of the two-plasmon decay instability in long-scale-length plasmas relevant to direct-drive inertial confinement fusion *Phys. Rev. Lett.* **108** 165003